

Interface and mechanical degradation mechanisms of the silicon anode in sulfide-based solid-state batteries at high temperatures

Qiuchen Wang(王秋辰), Yuli Huang(黄昱力), Jing Xu(许晶), Xiqian Yu(禹习谦), Hong Li(李泓), and Liquan Chen(陈立泉)

Citation: Chin. Phys. B, 2024, 33 (**8**): 088201. DOI: 10.1088/1674-1056/ad5276

What follows is a list of articles you may be interested in

Accurate estimation of Li/Ni mixing degree of lithium nickel oxide cathode materials

Penghao Chen(陈鹏浩), Lei Xu(徐磊), Xiqian Yu(禹习谦), and Hong Li(李泓)
Chin. Phys. B, 2024, 33 (**5**): 058202. DOI: 10.1088/1674-1056/ad3036

Atomistic understanding of capacity loss in $LiNiO_2$ for high-nickel Li-ion batteries: First-principles study

Shuai Peng(彭率), Li-Juan Chen(陈丽娟), Chang-Chun He(何长春), and Xiao-Bao Yang(杨小宝)
Chin. Phys. B, 2024, 33 (**5**): 058201. DOI: 10.1088/1674-1056/ad2a72

Liquid-phase synthesis of Li_2S and Li_3PS_4 with lithium-based organic solutions

Jieru Xu(许洁茹), Qiuchen Wang(王秋辰), Wenlin Yan(闫汶琳), Liquan Chen(陈立泉), Hong Li(李泓), and Fan Wu(吴凡)
Chin. Phys. B, 2022, 31 (**9**): 098203. DOI: 10.1088/1674-1056/ac7459

Analysis on diffusion-induced stress for multi-layer spherical core-shell electrodes in Li-ion batteries

Siyuan Yang(杨思源), Chuanwei Li(李传崴), Zhifeng Qi(齐志凤), Lipan Xin(辛立攀), Linan Li(李林安), Shibin Wang(王世斌), and Zhiyong Wang(王志勇)
Chin. Phys. B, 2021, 30 (**9**): 098201. DOI: 10.1088/1674-1056/ac11de

Imaging the diffusion pathway of Al^{3+} ion in NASICON-type $(Al_{0.2}Zr_{0.8})_{20/19}Nb(PO_4)_3$ as electrolyte for rechargeable solid-state Al batteries

Jie Wang(王捷), Chun-Wen Sun(孙春文), Yu-Dong Gong(巩玉栋), Huai-Ruo Zhang(张怀若), Jose Antonio Alonso, María Teresa Fernández-Díaz, Zhong-Lin Wang(王中林), John B Goodenough
Chin. Phys. B, 2018, 27 (**12**): 128201. DOI: 10.1088/1674-1056/27/12/128201

RAPID COMMUNICATION

Interface and mechanical degradation mechanisms of the silicon anode in sulfide-based solid-state batteries at high temperatures

Qiuchen Wang(王秋辰)[1,2], Yuli Huang(黄昱力)[1,2], Jing Xu(许晶)[1,2], Xiqian Yu(禹习谦)[1,2,3,†], Hong Li(李泓)[1,2,3,‡], and Liquan Chen(陈立泉)[1,2,3]

[1] *Key Laboratory for Renewable Energy, Beijing Key Laboratory for New Energy Materials and Devices, Beijing National Laboratory for Condensed Matter Physics, Institute of Physics, Chinese Academy of Sciences, Beijing* 100190, *China*

[2] *University of Chinese Academy of Sciences, Beijing* 100049, *China*

[3] *Huairou Division, Institute of Physics, Chinese Academy of Sciences, Beijing* 101408, *China*

(Received 9 May 2024; revised manuscript received 30 May 2024; accepted manuscript online 31 May 2024)

Silicon (Si) is a competitive anode material owing to its high theoretical capacity and low electrochemical potential. Recently, the prospect of Si anodes in solid-state batteries (SSBs) has been proposed due to less solid electrolyte interphase (SEI) formation and particle pulverization. However, major challenges arise for Si anodes in SSBs at elevated temperatures. In this work, the failure mechanisms of Si-Li_6PS_5Cl (LPSC) composite anodes above 80 °C are thoroughly investigated from the perspectives of interface stability and (electro)chemo-mechanical effect. The chemistry and growth kinetics of Li_xSi|LPSC interphase are demonstrated by combining electrochemical, chemical and computational characterizations. Si and/or Si–P compound formed at Li_xSi|LPSC interface prove to be detrimental to interface stability at high temperatures. On the other hand, excessive volume expansion and local stress caused by Si lithiation at high temperatures damage the mechanical structure of Si-LPSC composite anodes. This work elucidates the behavior and failure mechanisms of Si-based anodes in SSBs at high temperatures and provides insights into upgrading Si-based anodes for application in SSBs.

Keywords: sulfide electrolytes, silicon anodes, interface stability, degradation kinetics, all-solid-state batteries

PACS: 82.47.Aa, 82.33.Pt, 82.20.−w, 82.65.+r **DOI:** 10.1088/1674-1056/ad5276

1. Introduction

Solid-state batteries (SSBs) have been widely recognized as the next-generation energy-storage technology owing to nonflammability, potentially higher energy density and wide operating temperature.[1–8] In order to meet the ever-increasing requirements for high energy density and power density, it is urgent to employ high-capacity electrode materials and develop corresponding high areal-capacity and high-performance electrodes.[9]

Silicon (Si) has emerged as a very competitive alternative anode material in SSBs owing to its high theoretical capacity (3579 mAh·g^{-1} based on $Li_{15}Si_4$ at room temperature), low electrochemical potential (∼ 0.3 V vs. Li/Li$^+$) and high resource abundance.[10–12] Due to severe volume changes (∼ 300% for $Li_{3.75}Si$) during lithiation/delithiation, one major challenge Si faces in liquid electrolytes is continuous formation of SEI, leading to loss of lithium inventory, consumption of electrolyte and Si particle pulverization.[13] In contrast, Si anodes in SSBs could largely circumvent repeating SEI formation and particle pulverization because of the limited ductility of solid electrolytes and applied stack pressure. Specially, Si-anode SSBs using sulfide electrolytes (SEs) exhibit prominent performance.[10,14]

Despite promising broad prospects, Si anodes in SSBs still require improvement in terms of rate capabilities when compared to other anode alternatives. To our best knowledge, Si anodes in SSBs with areal capacity of 4 mAh·cm^{-2} could operate at a current density of 8 mA·cm^{-2} at most,[15] while Li-metal anodes can realize up to that of 155.3 mA·cm^{-2}.[16] In order to enhance electrode kinetics and thus fully exploit rate capabilities, elevating operating temperature is one of the most valid strategies,[10,17] by which graphite and $Li_4Ti_5O_{12}$ anode could operate at rates of 900 C and 1500 C at 100 °C, respectively.[18]

However, it is noteworthy that few studies have demonstrated cycling performance of Si anodes in SSB above 60 °C. Two crucial chemo-mechanical issues for Si anodes in SSBs at elevated temperature demand thorough research. (i) Interface stability is fundamental for cycling and rate performances, whereas opinions remain divided on the components of the Si|SE interphase. A prevalent assumption regarding the SEI formation mechanisms is mainly the reduction of SEs at low potential, for example, LPSC reduced to Li_2S, Li_3P and LiCl.[10,19,20] The SEI is passivating and tends to be stable after the few cycles. Yet a few studies suggest that the SEI originates from electrochemical reactions of Si and SEs and continues to grow, resulting in poor cycling performance and low coulombic efficiency.[21,22] A better understanding of the

†Corresponding author. E-mail: xyu@iphy.ac.cn
‡Corresponding author. E-mail: hli@iphy.ac.cn

© 2024 Chinese Physical Society and IOP Publishing Ltd

chemistry and growth rate of the Si|SE interface at elevated temperature is required. (ii) In SSBs, it is of paramount importance but also difficult to maintain interparticle contact, particularly at the anode side that would go through huge volume change during cycling. How the mechanical microstructure of Si anodes in SSBs evolves, especially in the first few activation cycles, largely influences the cell performance. It is worth of deep investigation whether contact loss, strain-stress cumulation or particle pulverization would happen at the Si|SE interface at elevated temperature.

In this work, we report the rapid degradation of Si-LPSC composite anodes at an elevated temperature of 80 °C. Our investigation delves into the failure mechanisms from two perspectives: the Li_xSi|LPSC interface stability and (electro)chemical-mechanical failure mechanisms of Si-LPSC composite anodes. The growth kinetics of the Li_xSi|LPSC interphase at 30 °C and 80 °C is contrasted through electrochemical impedance spectroscopy (EIS) measurement. Furthermore, the composition and the dependence of kinetic properties of interface products on temperature are investigated through experimental and computational methods. On the other hand, the contributions of SEI formation and electrode mechanical failure to capacity loss are elucidated by cross-sectional scanning electron microscopy (SEM) and titration gas chromatograph (TGC) method. These findings clarify the reasons for vigorous SEI growth and the detrimental effects of local electrode stress induced by the excess lithiation of Si in SSBs at elevated temperatures.

2. Results and discussion

2.1. Electrochemical performances of Si-LPSC composite anodes at high temperature

Initially, to evaluate the interfacial compatibility between Si anodes and sulfide electrolyte Li_6PS_5Cl at different temperatures, the electrochemical performance of half-cells with Si-LPSC composite anodes was measured at 30 °C, 60 °C, and 80 °C (Fig. 1). The mixture of nano-sized silicon (nm-Si) powder and LPSC was used as the research object of investigation (Fig. 1(a)) instead of 100% Si.[23] The three main reasons are as follows. Firstly, by turning two-dimensional (2D) interface into a three-dimensional (3D) one, the contact area would be enlarged. Then, side interactions at the Si|LPSC interface could be greatly magnified and thus easier to observe. Secondly, Si exhibits low ion diffusivity,[23] severely limiting its rate capability, and a simple method to tackle this problem is to form a Si-SE composite. Lastly, SE plays an important role as a skeleton to alleviate huge volume change during lithiation/delithiation process of Si ($\sim$ 300%). Mixture of different ratios of nm-Si to LPSC was tested to choose the best research object, and it turned out that the corresponding half-cells exhibited the best cycle stability when the mass ratio of nm-Si and SE was 30:70 (Fig. S1).

Raising operating temperature is one of the most effective approaches to optimizing electrode kinetics and thus enabling larger charge/discharge capacities at ultrahigh rates. especially for SSBs. However, it seems that 60 °C is a turning point of Si-LPSC anode electrochemical capabilities. As shown in Fig. 1(b), the cycling performances of half-cells with Si-LPSC anodes operating at 80 °C fail those working at 30 °C and 60 °C. The half-cells operating at 30 °C and 60 °C exhibit stable cycling performances and much higher coulombic efficiency, retaining 83.4% and 84.1% of their initial capacities after 50 cycles, respectively. While the behavior of Si-SE cell at 80 °C is noticeably different: the charge capacity is far lower since the first cycle, and the capacity retention fades dramatically to 14.3% after 50 cycles.

In the first cycle, the discharge capacities at 30 °C, 60 °C, and 80 °C are 3481.5 $mAh{\cdot}g^{-1}$, 3718.2 $mAh{\cdot}g^{-1}$, and 3970.9 $mAh{\cdot}g^{-1}$, respectively, increasing with temperature (Fig. 1(c)), while their initial charge capacities are 3051.6 $mAh{\cdot}g^{-1}$, 3169.7 $mAh{\cdot}g^{-1}$, and 2339 $mAh{\cdot}g^{-1}$, respectively, reaching the maximum value at 60 °C. Although the discharge/charge plateaus are similar at different temperatures, the initial coulombic efficiencies (ICE) decrease with temperature, namely, 87.6% at 30 °C and 58.9% at 80 °C. In the 50th cycle (Fig. 1(d)), despite the discharge/charge curves of cells at 30 °C and 60 °C maintain well, the counterpart at 80 °C exhibits severe polarization. As shown in Fig. 1(e), the polarization voltage of Si-LPSC composite anodes decreases with elevated temperature because of the improved electrode kinetics in the first few cycles. However, it remains barely the same after cycle at 30 °C and 60 °C, but grows rapidly at 80 °C. Furthermore, contrary to common situation,[18] raising the temperature beyond 80 °C deteriorates the rate capabilities of Si-LPSC composite anodes (Fig. S2(a)), suggesting that the enhancement of elevating temperature on improving SSB rate capacities is limited. Summarizing these electrochemical results, it is indicated that interfacial reaction and mechanical failure of Si-LPSC anode cause dramatic capacity decrease at temperature above 80 °C.

To elucidate the correlation between electrode kinetics and temperature, it is essential to examine the ionic and electronic conductivities of the Si-LPSC composite anode at different temperatures. Given that this electrode serves as a mixed ionic–electronic conductor, ion-blocking cells and electron-blocking symmetric cells as illustrated in Figs. S3(a) and S3(b) were assembled to determine the electronic and ionic conductivities of the composite anodes via the direct current (DC) polarization method. As depicted in Fig. S3(c), the electronic conductivity of the Si-LPSC composite anode is positively correlated with temperature, attributing to the

temperature-dependent electronic properties of Si as a semiconductor. Conversely, the ionic conductivity shows a negative correlation with temperature, contrary to the characteristics of sulfide solid electrolytes LPSC itself, indicating significant interfacial reactions, suggesting that Si is intrinsically unstable to LPSC. The DC polarization test lasts for 80 hours, thereby allowing ample time for the interfacial reactions to proceed.

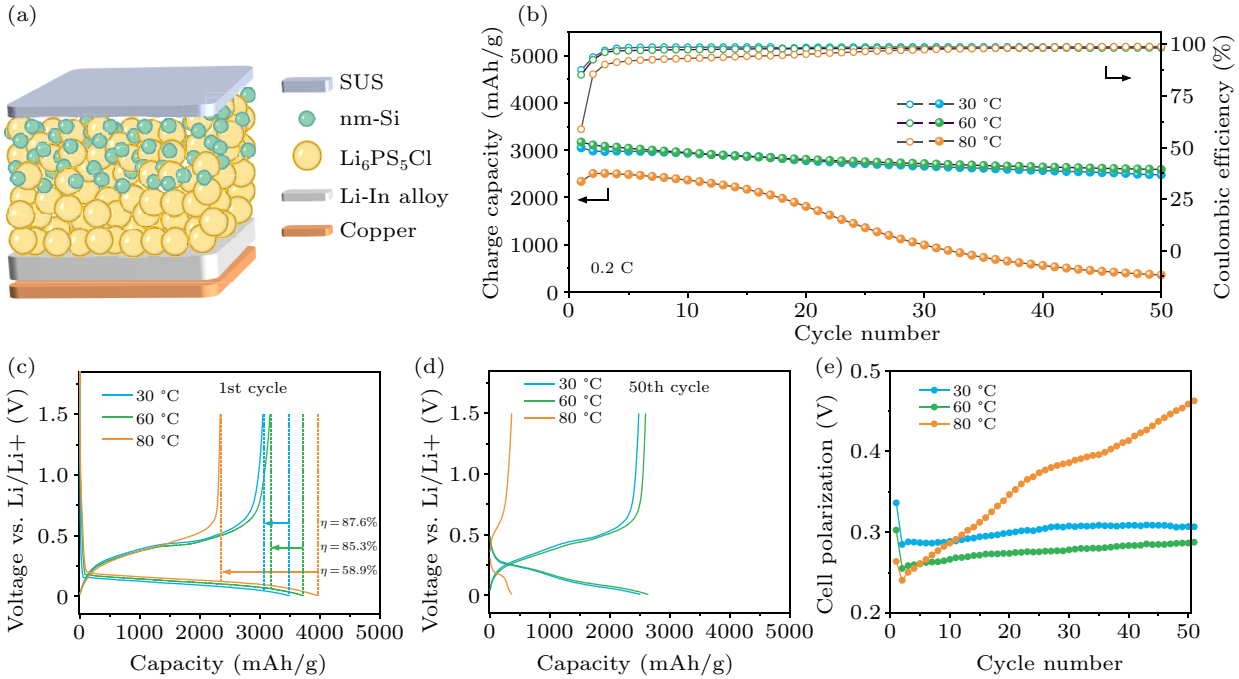


Fig. 1. Electrochemical performance of Si-LPSC anodes at different temperatures. (a) The schematic of Si-LPSC||Li–In half-cell. (b) Cycling performances, charge/discharge profiles in the (c) 1st and (d) 50th cycle and (e) polarization voltage of Si-LPSC||Li–In half-cells at 0.2 C at 30 °C, 60 °C and 80 °C.

The differential capacities with cell potential (dQ/dV) curves in the first two cycles at 30 °C and 80 °C are plotted in Figs. S2(b) and S2(c) to clarify the role that LPSC plays in the lithiation/delithiation process of the composite anode. In the first discharge, only one peak at ∼ 0.1 V is observed, indicating the formation of amorphous Li_xSi.[24,25] In the following delithiation process, two peaks at 0.36 V and 0.44 V are attributed to the phase transition from $Li_{13}S_4$ to Li_7Si_3 and then to LiSi.[26] Correspondingly, two peaks at 0.08 V and 0.25 V in the second discharge are ascribed to the converse transition from LiSi to Li_7Si_3 and then to $Li_{13}S_4$.[26] The peaks in the second charge are nearly the same as those in the first charge. Since no pronounced peaks are observed above 1.0 V, the redox of LPSC itself can be omitted.[27] In other words, the electrochemical reaction processes here are all about Si lithiation/delithiation.

In addition, the redox of LPSC at different temperatures is investigated. LPSC serves as redox-active material and 5 wt.% carbon additives are utilized to enlarge reduction/oxidation current. As depicted in Fig. S4, the LPSC-carbon anode delivers the initial reduction/oxidation capacity of 411.4 mAh·g^{-1} and 50.3 mAh·g^{-1} at 30 °C and 664.4 mAh·g^{-1} and 193.8 mAh·g^{-1} at 80 °C. Raising temperature does aggravate the redox of LPSC, but the result that the irreversible capacity and coulombic efficiency of SE redox at 80 °C are higher than those at 30 °C disagrees with the cycle performance of Si-LPSC composite anodes. Hence, LPSC redox is not the main reason for the deterioration of Si-LPSC anodes at high temperature.

Summarizing the above electrochemical performances, it can be inferred that the severe deterioration of the performance of Si-LPSC composite anode at high temperatures of 80 °C and above is caused by the interfacial chemical/electrochemical instability and mechanical failure at high temperatures. Several possible causes of failure will be deeply discussed.

2.2. Temperature-dependent interface degradation mechanism

2.2.1. Transition of interface resistance growth kinetics

To investigate the impact of interfacial degradation on the cell cycling performances at high temperatures, the evolution of impedance with cell resting time was monitored. The Si|Li-In half-cells were discharged to 0.005 V (vs. Li^+/Li) at 30 °C and 80 °C, and then fully rested at the same temperatures, respectively. During the cell resting period, impedance test was performed every 24 h. An anode composed of 100 wt.% nano-Si is used here instead of a Si-LPSC composite anode so that the electrode interfaces to be studied would be com-

pressed from 3D to 2D. It helps simplify the impedance analytics and concentrate on the interfacial reaction between Li_xSi and LPSC by largely eliminating the impact of mechanical structure evolution and LPSC oxidation/reduction.

Figures 2(a) and 2(d) depict the stacked Nyquist plots at different cell resting time, and the points at frequencies of 5000 Hz and 0.05 Hz are marked by dashed lines. The Nyquist plots basically maintain a similar shape over time, but impedance growth rates are quite different at 30 °C and 80 °C. The semicircle between 5000 Hz and 0.05 Hz is attributed to the Li_xSi|LPSC interface resistance, denoted as R_{int}. For SSBs based on inorganic solid electrolytes, R_{GB} and $R_{SE,bulk}$ represent grain boundaries and bulk resistance of SE pellet and correspond to the semicircle at high frequency and the interception. The Warburg tail at low frequency indicates the ion diffusion in Li_xSi alloy.

As explained above, the equivalent circuit for EIS analysis is R(RQ)(RQ)Q. The fitting results in Figs. 2(b) and 2(e) exhibit that R_{int} at 30 °C mildly increases from 59 Ω to 195 Ω after resting for one week and tends to become stable in the end, while R_{int} at 80 °C drastically increases from 893 Ω to 8029 Ω at an accelerated rate.

Since EIS measurements were conducted during cell resting instead of cycling, the interface impedance growth is supposed to originate from interface characteristics. At moderate temperatures like 30 °C, the Li_xSi|LPSC interface is close to an electron-insulating layer, which inhibits the interfacial reaction upon SEI formation. In contrast, the Li_xSi|LPSC interface impedance grows drastically at 80 °C, indicating that the interface is non-passivating. The interface layer is a mixed ionic/electronic conductor, hence the interfacial reaction continues to take place and the interface grows persistently.[28,29] Intuitive schematic diagrams are depicted in Figs. 2(c) and 2(f). The reason for the transition of interface resistance growth kinetics will be investigated later.

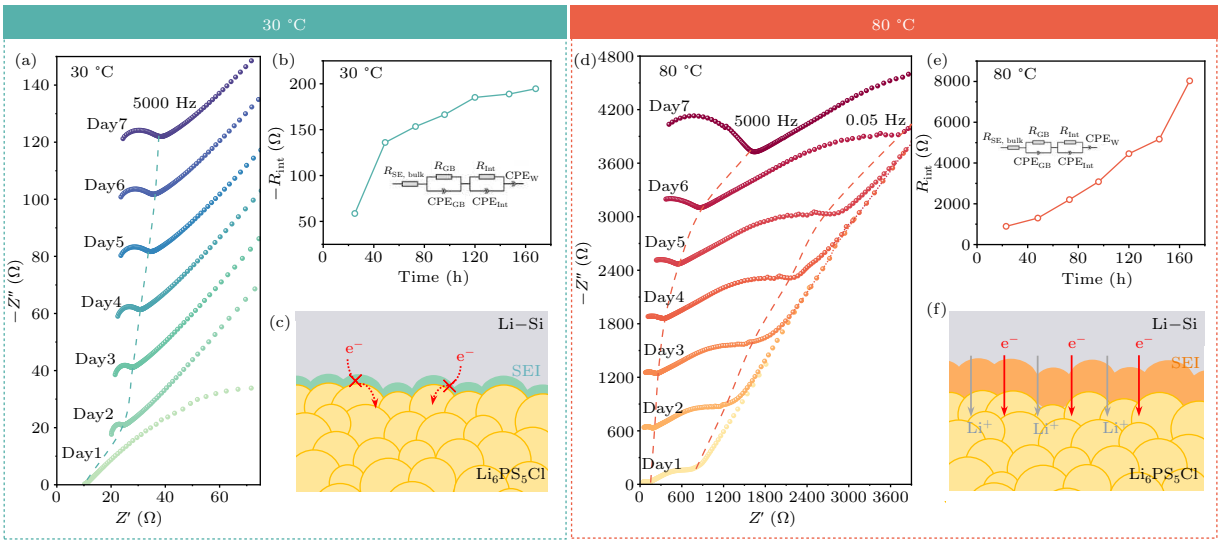


Fig. 2. Impedance measurements of a half-cell with Si-LPSC composite anode after discharging to −0.615 V vs. In/InLi (i.e., 0.005 V vs. Li^+/Li). [(a) and (d)] Nyquist plots of a typical cell with long-term resting at 30 °C and 80 °C, respectively. [(b) and (e)] The Li_xSi|LPSC interface resistance R_{int} as a function of time. The insets in panels (b) and (e) are the corresponding equivalnet circuits for EIS fitting. [(e) and (g)] Interface resistance growth as a function of the square of time. [(c) and (f)] The schematic diagrams of different mechanisms of SEI growth.

2.2.2. Chemical characterization of Li_xSi|LPSC interphases

To determine the chemistry of the SEI by experiment, we measured *ex-situ* x-ray photoelectron spectroscopy (XPS) spectra of composite anodes before and after cycled at 30 °C and 30 °C respectively. All XPS spectra are charge-calibrated based on C 1s peak at 284.8 eV and demonstrated in Figs. 3(a)–3(c).

The Si 2p XPS spectra before and after cycling are contrasted in Fig. 3(a). Prior to cycling, peaks corresponding to Si–O or Si–P were observed for the Si-LPSC composite anode. These peaks could be the result of Si|LPSC interface products that were first formed during the cell resting process, or they could be the result of the oxide layer on the surface of the Si nanoparticles. Five weeks of cycling at 30 °C resulted in a considerable drop in the Si peak intensity and a notable enhancement of the Si–P peak. The peak intensity ratio of the Si peak to the Si–P peak further decreased following cycling at 80 °C.

Figures 3(b) and 3(c) display the P 2p and S 2p XPS spectra of the Si-LPSC composite anodes, respectively. Before cycling, the peak of PS_4^{3-} was present. Si–P and Li_2S peaks showed up with a rather low percentage after cycling at 30 °C; however, after cycling at 80 °C, their percentage increased noticeably in comparison to PS_4^3. According to all of these results, the Li_xSi|LPSC interfacial reaction appears to be intensifying at high temperatures.

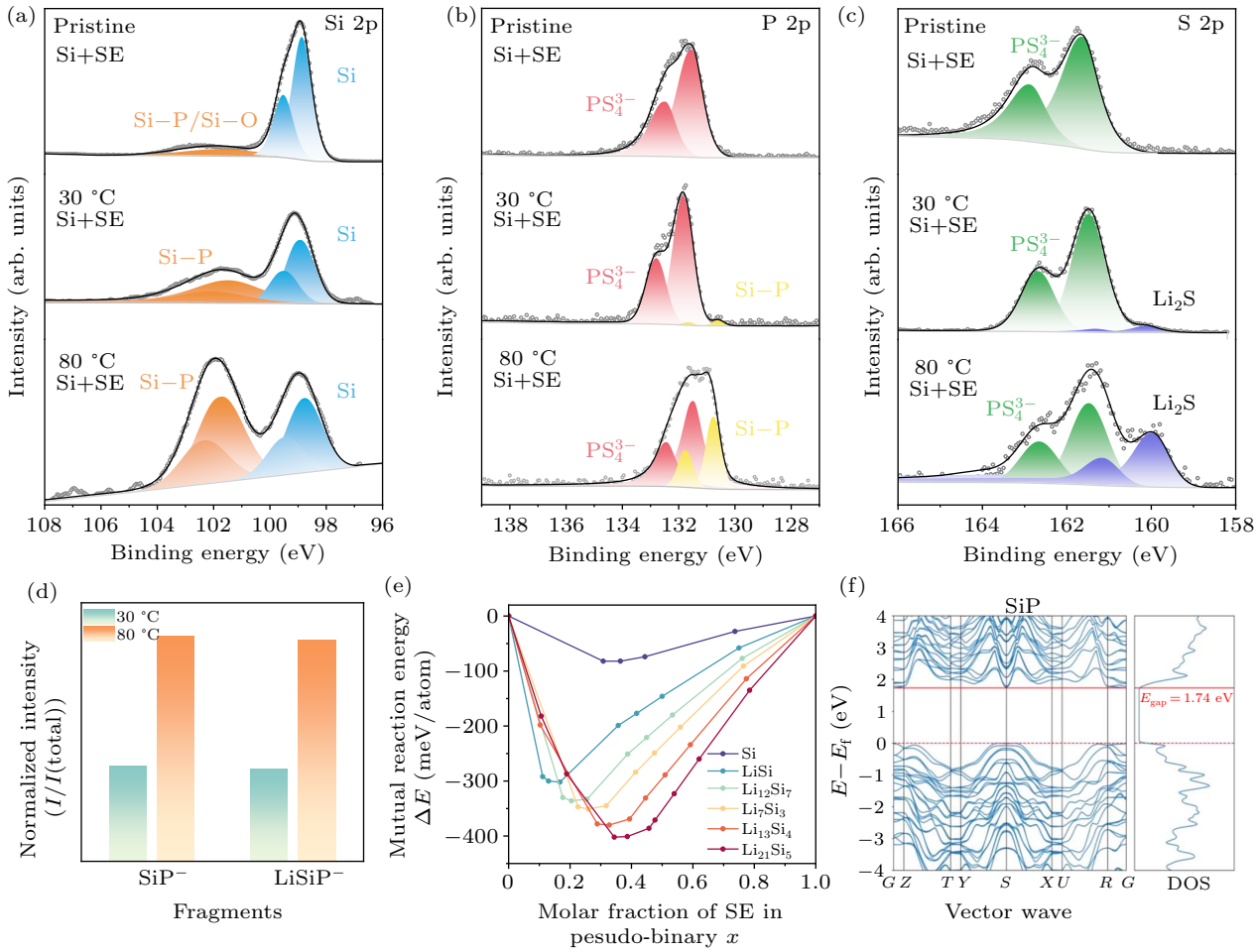


Fig. 3. *Ex situ* XPS spectra of (a) Si 2p, (b) P 2p and (c) S 2p from Si-LPSC anodes before and after cycled at 30 °C and 80 °C respectively. (d) Normalized intensity of SiP and LiSiP fragments. (e) Calculated chemical reaction energy of Li_xSi ($x = 0$–4.4) and LPSC as a function of LPSC molar ratio. (f) Calculated band structure and density of state (DOS) of SiP.

ToF-SIMS spectrum depicted in Fig. 3(d) shows that the counting of SiP and LiSiP fragments, as well as those of $LiSiP_2$, Li_3SiP_2, SiP_2, SiP_3, Li_4SiP_2 and Li_2SiP_3 fragments (Fig. S5), were significantly higher after cycling at 80 °C for the Si-LPSC anodes. The presence of Si–P bonds and semiconductor nature of all these products indicate that at least one of the semiconductors SiP, Li_5SiP_3, and SiP_2 is present in the Li_xSi|LPSC interphases. Furthermore, the increasing content of these semiconductors with temperature suggests an intensification of the interfacial reaction.

2.2.3. First principles calculation on the Li_xSi|LPSC interphases

Theoretically, first principles calculation was employed to provide a more detailed understanding of the composition and characteristics of the Li_xSi|LPSC interphases.[30] The interface was regarded as a pseudo-binary system, and compositional phase diagrams were created to assess the interfacial reactions. The thermodynamic phase equilibria of the Li_xSi|LPSC interface were assessed by calculating the reaction energy ΔE_R,[30] which does not include the decomposition energies of Li_xSi and LPSC individually.[31] The most thermodynamically favorable reaction pathway is the one in which the reaction energy reaches the minimum, denoted by $\Delta E_{R,min}$. The normalized reaction energies between Si/LiSi/$Li_{12}Si_7$/Li_7Si_3/$Li_{13}Si_4$/$Li_{21}Si_5$/$Li_{22}Si_5$ and LPSC, as shown in Fig. 3(e) and Table 1, are −0.114 eV/atom, −0.309 eV/atom, −0.341 eV/atom, −0.357 eV/atom, −0.383 eV/atom, −0.397 eV/atom, −0.407 eV/atom and −0.412 eV/atom. The result indicates that both Si and Li–Si alloys have a thermodynamic inclination to react with LPSC, which becomes more pronounced as increased lithium is embedded in Si particles. This aligns with the conventional perception that the higher the concentration of lithium in the alloy-type anode, the greater its chemical reactivity.

Although the actual Li_xSi|LPSC interphases may differ from the calculation results and may not be evenly distributed along the normal direction of the interface, the calculation results strongly suggest that the interfacial reactions between Li_xSi anodes and LPSC, though may be kinetically limited at moderate temperatures (60 °C and below), could lead to severe cell deterioration after aging or cycling at high temperatures (80 °C and above), which is also supported by the experimental findings.

It is noteworthy that the characteristics of the interphases are more significant than the inherent chemical/electrochemical stability between the electrode and electrolyte. Table 1 displays the interfacial products of LPSC and Si with varying degrees of lithiation, all containing Si or Si–P compounds (i.e., SiP, Li_5SiP_3, and SiP_2). Density functional theory (DFT) calculations of the electronic band structure and density of states (DOS) of these components were undertaken, and results shown in Figs. 3(f) and S6 indicate that Si or Si–P compounds are all semiconductors, with band gaps of 1.74 eV, 1.32 eV, 1.43 eV and 0.61 eV, respectively. The carrier concentration in semiconductors is positively associated with temperature when at or near room temperature according to the following equation:[32]

$$n_e = AT^{3/2} e^{-\Delta E_g/(2kT)}. \quad (1)$$

Given that the electronic conductivity of semiconductors is approximately proportional to the carrier concentration, with temperature rising, the SEI containing SiP, Li_5SiP_3, SiP_2 or Si changes from electronic insulting interfaces to ones that consist of mixed ionic and electronic conductors (MIEC),[29] making the interfacial degradation no longer self-limiting. Hence, the reaction kinetics get intensified at high temperature, which explains why the interface resistance is getting larger with the aging or cycling duration.

Table 1. Thermodynamic phase equilibria and reaction energies of the Li_xSi|LPSC ($x = 0$–4.4) interface.

C_{SE}	C_{anode}	Phase equibiliria				$\Delta E_{R,min}$ (meV per atom)
Li_6PS_5Cl	Si	SiP	Li_2SiS_3	LiCl	Li_2S	−0.114
	LiSi	SiP	Si	LiCl	Li_2S	−0.309
	$Li_{12}Si_7$	Li_5SiP_3	Si	LiCl	Li_2S	−0.341
	Li_7Si_3	Li_5SiP_3	Si	LiCl	Li_2S	−0.357
	$Li_{13}Si_4$	Li_5SiP_3	Si	LiCl	Li_2S	−0.383
	$Li_{15}Si_4$	Li_5SiP_3	Si	LiCl	Li_2S	−0.397
	$Li_{21}Si_5$	Li_5SiP_3/Li_3P	Si	LiCl	Li_2S	−0.407
	$Li_{22}Si_5$	Li_5SiP_3/Li_3P	Si	LiCl	Li_2S	−0.412

2.3. Influence of temperature on mechanical fractures and structure evolution of composite anodes

(Electro)chemo-mechanics plays a prominent role in ASSBs because of rigid solid/solid contacts interactions, which is largely responsible for ASSB failure. Severe volume change of Si during lithiation/delithiation poses a great challenge from the mechanics standpoint and the underlying (electro)chemo-mechanical mechanisms remain ambiguous. Cross-sectional SEM and EDS were employed to study the structure evolution of Si-LPSC composite anode.

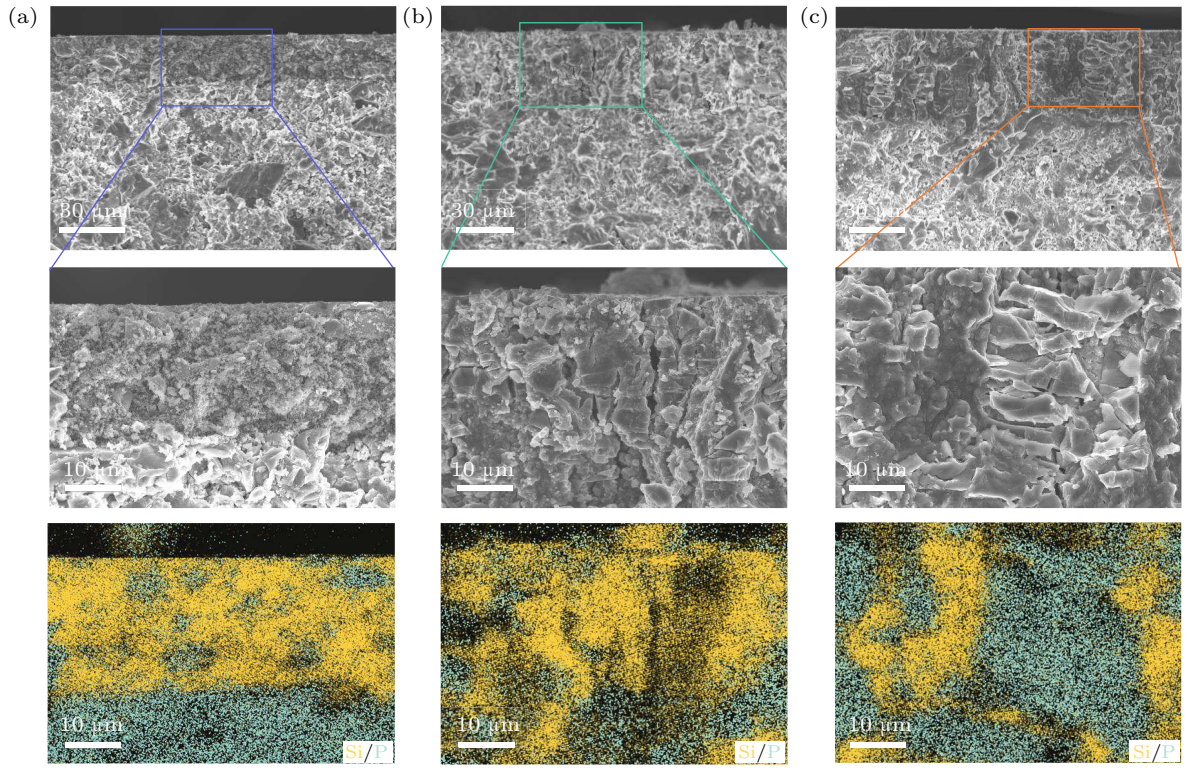


Fig. 4. Cross-sectional SEM images and EDS mapping of Si-LPSC|LPSC|Li–In cells before (a) and after 1 cycle at 30 °C (b) and 80 °C (c).

Figure 4(a) displays the cross-sectional SEM of pristine Si-LPSC composite anode. The pristine composite anode is highly dense with nm-Si and solid electrolyte LPSC uniformly dispersed. The well-balanced ratio of the active material Si to the superior ionic conductor LPSC ensures optimal contact area and a highly stable electrode skeleton at room temperature. As can be observed from the EDS mapping, the elements Si and P are uniformly distributed, illustrating no obvious seg-

regation of the Si and LPSC. The good mechanical strength and fast Li^+ diffusion ability of the LPSC electrolyte lay a solid foundation for electrons and ions transport throughout the electrode and thus are beneficial for the battery capacity to be fully exploited and well maintained.

The cross-sectional SEM images of the Si-LPSC composite anode after 1 cycle at 30 °C (Fig. 4(b)) show several tiny cracks perpendicular to the electrolyte layer in some localized areas. Although these cracks seem to cause localized damage to the mechanical structure, they did not significantly affect the overall electrochemical performance because the longitudinal cracks would scarcely hinder the ionic and electronic conduction from solid electrolyte separator to current collector.[10] From the magnified SEM images and EDS mapping, it can be seen that these longitudinal cracks mainly occur in Si and are supposed to arise from the substantial volume change of Si during the lithiation/delithiation process. Despite the occurrence of cracks, the distribution of Si and P elements is still rather uniform, demonstrating that the ion and electronic transport networks in the electrode are well maintained after cycling at ambient temperature.

In contrast, figure 4(c) displays a quite different behavior of the Si-LPSC composite anode after cycling at 80 °C. As indicated by the cross-sectional SEM, considerable cracks parallel to the electrolyte layer form in the Si-LPSC anode after one cycle at 80 °C. The cracks are caused by the radical volume expansion and contraction of Si and continuous interfacial reactions, which disrupt the local ion/electron transport network and, as a consequence, result in a rapid capacity loss and a rather low ICE. According to the EDS mapping, the transverse cracks are primarily generated within the LPSC particle. This is presumed to be the result of the excessive internal stress of the electrode with the space limitation of cell mold and the violent expansion of Si. The internal stress exceeds the yield strength of the LPSC, leading to the deactivation of a significant amount of Si. In addition, the Si appears to agglomerate and thus its contact area with the electrolyte becomes smaller. Both a substantial number of transverse cracks and the aggregation of Si account for the rapid capacity decline of Si-LPSC half-cells at 80 °C.

The preceding results demonstrate the failure mechanisms of Si-LPSC composite anode under high-temperature circumstances from the perspective of (electro)chemical-mechanics.

2.4. The combined effect of interfacial reactions and electrode mechanical damage

2.4.1. Trapped Li_xSi and SEI Li^+ quantified by TGC method

As previously discussed, both interfacial reactions and electrode mechanical failure have a negative impact on the electrochemical behavior of Si-LPSC anodes. In order to distinguish the inactive SEI Li^+ from trapped Li_xSi alloy and correlate them with the cell performance, titration gas chromatography (TGC) method was adopted to quantify active Li_xSi alloy by aprotic solvent.[33]

Considering that H_2S formed by the reaction of LPSC and H_2O could corrode the TGC equipment, anhydrous ethanol was used as the solvent for titration instead. Previous work has demonstrated that ethanol can serve as the titrant for silicon anodes.[34] The half cells with Si-LPSC anodes were disassembled to perform the TGC test after being discharged/charged with a current density of 0.3 mA/cm^2. Once the H_2 amount is quantified based on the calibration curve, the corresponding trapped Li_xSi alloy content could be obtained based on

$$2Li_xSi + 2xH^+ \rightarrow 2xLi^+ + 2Si + xH_2\uparrow. \tag{2}$$

Then, Li^+ content in the electrochemically formed SEI could be determined based on

$$Q_{SEI} = Q_{total} - Q_{Li_xSi}, \tag{3}$$

where Q_{total} corresponds to the capacity loss.

As depicted in Fig. 5(a), the normalized Li^+ content consumed for SEI formation after the first lithiation process at 80 °C is more than that at 30 °C. It is well consistent with the aforementioned impedance growth and further proves that the Li_xSi|LPSC interface reaction is intensified at high temperature. Besides, the capacity contribution from Li_xSi alloy during the first lithiation at 80 °C is slightly larger than that at 30 °C (Fig. 5(b)). Enhanced kinetics at elevated temperature benefits the full utilization of capacity of silicon anodes, but also results in a greater proportion of amorphous $Li_{15}Si_4$ (a-$Li_{15}Si_4$) transmitting into crystalline $Li_{15}Si_4$ (c-$Li_{15}Si_4$) and therefore more severe volume change. Moreover, c-$Li_{15}Si_4$ has a higher Young's modulus than a-$Li_{15}Si_4$,[35–37] thus the internal local stress of Si-LPSC anodes would notably increase with external pressure applied to the SSB mold. When it reaches beyond the critical point that corresponds to the yield strength of LPSC particle, full lithiation of Si would cause LPSC particles to break, which echoes with the cross-sectional SEM images of composite anodes cycled at 80 °C (Fig. 4(c)).

Surprisingly, capacity loss from trapped Li_xSi far surpasses that from SEI formation in the first cycle at 80 °C, while the contribution from the two parts is very close at 30 °C (Figs. 5(c) and 5(d)). It reveals that after the initial lithiation, excessively expanded Li_xSi alloy at 80 °C becomes incapable of adequate delithiation and causes instant failure of the electrode mechanical structure, which explains why the coulombic efficiency is particularly low in the first cycle. The damaged electrode structure laid a poor foundation for Si-LPSC anode cycling at 80 °C.

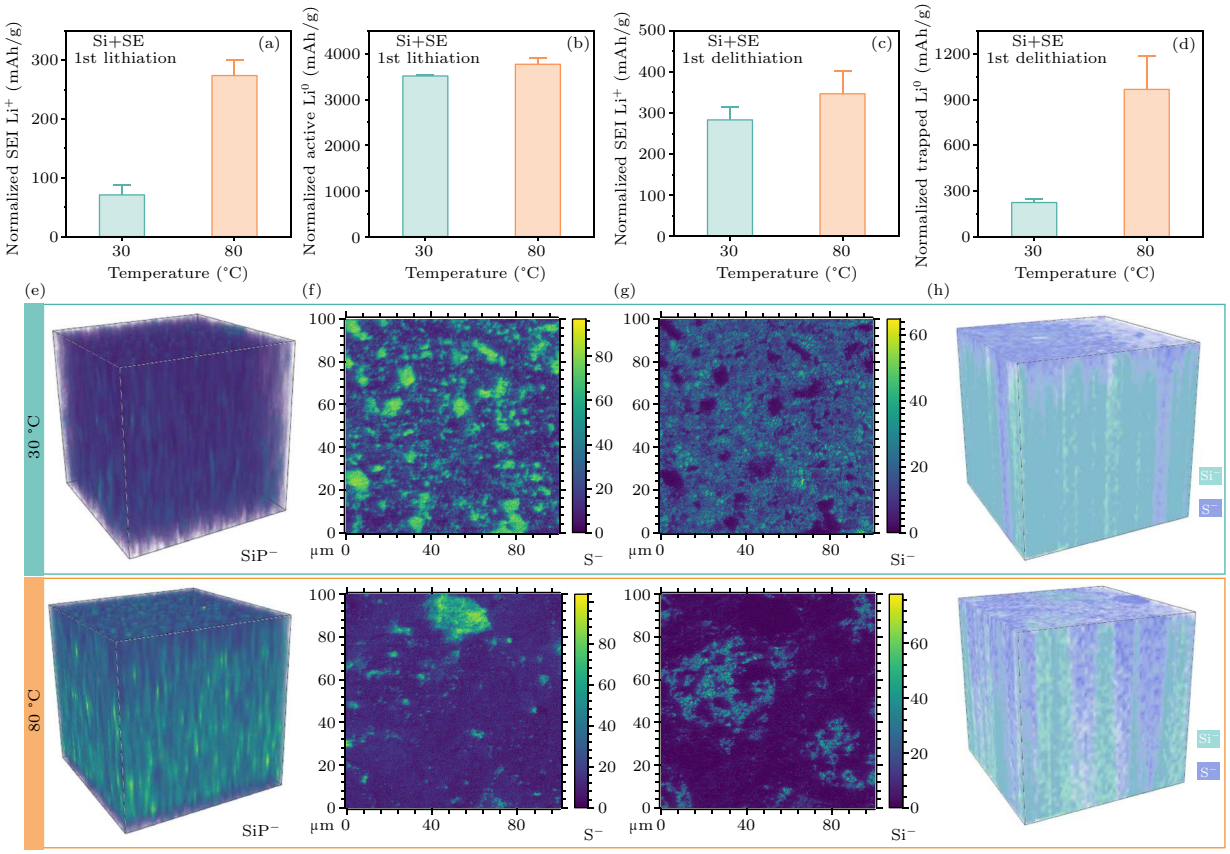


Fig. 5. Quantification of the normalized Li loss from [(a) and (c)] SEI Li^+ and [(b) and (d)] trapped Li_xSi after first lithiation/delithiation at 30 °C and 80 °C via the TGC method. ToF-SIMS results of Si-LPSC composite anodes after 50 cycles at 30 °C and 80 °C. (e) 3D distribution of SiP, 2D distribution of (f) S and (g) Si, and (h) 3D distribution of S and Si in the Si-LPSC composite anodes cycled at 30 °C and 80 °C respectively.

2.4.2. Trapped Li_xSi and SEI Li^+ quantified by TGC method

The spatial distribution of SiP, a representative kind of fragments of the Li_xSi|LPSC interphases, is shown in Fig. 5(e). In the Si-LPSC anode cycled at 30 °C, SiP is barely visible, while the content of SiP in 80 °C cycled anode increases significantly and its spatial distribution is rather homogenous.

The 2D planar distributions of the representative S and Si fragments, corresponding to Li_xSi and LPSC, are shown in Figs. 5(f) and 5(g). At 30 °C, S is uniformly and discretely distributed, which is highly congruent with cross-sectional SEM images (Fig. 4(b)), whereas Si exhibits a much smaller particle size than S and uniformly fills in the surrounding area of S, which is quite similar to the structure of composite anode before cycling (Fig. 4(a)). In contrast, after 80 °C cycling, both S and Si show aggregation, probably due to the segregation caused by the drastic volume change of Si.

Combining the spatial distribution of S and Si, the results are shown in Fig. 5(h), where the blank part corresponds to the cracks inside the composite anode. The increased cracks and pores in the composite anode after cycling at 80 °C further support that the huge internal stress of the composite anode results in the serious mechanical deterioration.

3. Conclusion

In summary, by combining experimental and computational approaches, we systematically investigate the interface and mechanical failure mechanisms of Si-LPSC composite anodes at high temperatures. Severe electrochemical degradation of Si-LPSC anodes can be observed during cycling at 80 °C, leading to inferior ICE and capacity retention. EIS measurements were conducted to monitor the interfacial resistance growth at 30 °C and 80 °C respectively. The results from *ex situ* XPS, ToF-SIMS and computation have confirmed the existence of semiconductor Si and/or Si–P compound in the Li_xSi–Li_6PS_5Cl interphases, which causes the interface to turn to non-passivating at elevated temperatures. On the other hand, the role of (electro)chemo-mechanics at 3D Li_xSi|LPSC interfaces on capacity fading of SSBs is thoroughly elucidated. Contact loss, strain-stress accumulation, SE particle pulverization and Si segregation at high temperatures do irreversible damage to electrode structure and cell kinetics. This work provides novel insights for the next-level development of Si anodes in SSBs, especially for application in a wide-temperature range.

Appendix A: Experiments

A1. Preparation of composite anode and cell assembly

For the anode active materials, nano-silicon powder ($D_{50} \approx 100$ nm) and Li_6PS_5Cl powder ($D_{50} = 5$ μm–10 μm) were purchased from Tianmulake Excellent Anode Materials Co., Ltd and Hefei Kejing Materials Technology Co. Ltd., respectively. The composite anode was fabricated by mixing nm-Si and SE at different weight ratios (2:8, 3:7, 4:6, 5:5) and hand ground in a mortar for at least 30 min.

For cell assembly, 80 mg Li_6PS_5Cl was first placed into the mold and pressed at 120 MPa (1 ton) to form a pellet. Composite anode powder with areal loading of ~ 2.5 mg was put on the top and dispersed uniformly, then an In foil (Alfa Aesar, 10 mm diameter, ~ 10 μm thickness) and a Li foil (China Energy Lithium Co., Ltd., 9.5 mm diameter, ~ 10 μm thickness) were placed under the SE pellet. The cells were pressed at 360 MPa (3 tons) for 3 min and cycled under a stack pressure of about 30 MPa. All the preparation processes were performed in an argon-filled glovebox ($O_2 > 0.1$ ppm, $H_2O > 0.1$ ppm).

A2. Electrochemical characterization

A2.1. Cell cycling and rate performances

Galvanostatic charge–discharge of Si|Li-In half-cells was conducted in a voltage range of $-0.615 \sim 0.88$ V vs. In/InLi (i.e., $0.005 \sim 1.5$ V vs. Li^+/Li) via battery test system (LAND, CT2001A) at 30 °C, 60 °C and 80 °C respectively. The cycling test was performed at 0.2 C and the rate test was conducted at 0.1 C to 2 C. EIS measurements were performed in a climate chamber (Binder) at the temperatures of 30 °C, 60 °C, and 80 °C to mitigate the influence of temperature on impedance variations. The cell was discharged to -0.615 V vs. In/InLi (i.e., 5 mV vs. Li^+/Li) with a current density of 600 $mA \cdot g^{-1}$ (0.2 C). During resting, EIS was conducted every 24 h. The impedance spectra were measured by applying 10 mV amplitude in a frequency range of 1 MHz–0.1 Hz with 20 points per decade. All Nyquist plots were fitted with R(RQ)(RQ)Q equivalent circuit. According to the fitting results, we plotted the resistance of the anode/electrolyte interface with time.

A2.2. Ionic and electronic conductivity tests of composite cathodes

DC polarization methods were utilized to assess the ionic and electronic conductivities of composite anodes.[38] Two distinct symmetric cell configurations, namely, ion-blocking and electronic-blocking cells, were selected to measure the ionic and electronic conductivities, respectively. To ensure adequate thickness of composite anode pellets, the anode mixtures were weighted at 100 mg. For electronic conductivity evaluations, the anode composites underwent compression at 360 MPa for 5 min between two stainless steel cylinders to form the ion-blocking cells. For ionic conductivity assessments, five-layer electronic-blocking cells (Li–In|LPSC|composite anode|LPSC|Li–In) were constructed. Initially, the anode composites were pressed at 200 MPa. Subsequently, 60 mg of LPSC powders were pressed on both sides of the composite cathode layers at 200 MPa. Li–In foils were affixed to each side and pressed at 360 MPa. The cell was maintained at a constant external pressure of 30 MPa throughout the tests. With a DC voltage of 0.3 V applied, the corresponding current response was recorded. Ohm's law ($U = I \times R$) was employed to determine the partial resistances, where current values (I) were obtained by fitting the steady-state region. Ionic and electronic conductivities were calculated based on the equation

$$\sigma = L/(RA), \tag{A1}$$

where L, R and A represent thickness, resistance, and area of composite anode layers, respectively.

A3. Chemical and morphological characterization

X-ray photoelectron spectroscopy (XPS) The XPS of the cycled electrodes was carried out by ESCALAB 250 Xi Thermo Fisher with monochromatic 150 W Al $K\alpha$ radiation. Cycled composite anode samples were prepared from half-cells after 5 cycles.

Cross-sectional SEM Cross-sectional morphology of composite anodes was characterized by scanning electron microscope (SEM, HITACHI S4800). Cycled composite anode samples were prepared from half-cells after 1 cycle.

Titration gas chromatography (TGC) TGC experiments utilized a Shimadzu GC-2010 Plus Tracera with a barrier ionization discharge (BID) detector. Operating conditions included a split temperature of 200 °C with a split ratio of 2.5 (split vent flow: 20.58 ml/min, column gas flow: 8.22 ml/min, purge flow: 0.5 ml/min). The column temperature (RT-Msieve 5A, 0.53 mm) was maintained at 40 °C, while the BID detector temperature was set at 235 °C. Helium (99.9999%) served as the carrier gas, with a BID detector gas flow rate of 50 ml/min. An Ar-filled glove box housed the anode sample within a septum glass vial. Following the injection of 0.5 mL anhydrous ethanol, 30 μL sample gases were introduced into the machine via a 50 μL Gastight Hamilton syringe.

ToF-SIMS To prevent exposure to the ambient atmosphere, the transfer of the sample from the glovebox to the SIMS instrument was carried out using a Leica EM VCT500 shuttle (Leica Microsystems GmbH) under vacuum. ToF-SIMS characterizations were performed using a Hybrid SIMS M5 system (IONTOF GmbH in Münster, Germany). The measurements were performed in negative ion mode. The analysis region was defined as a square of 100 μm × 100 μm. The Surface Lab 7.1 software (IONTOF GmbH, Münster, Germany) was employed for the measurement and assessment of data.

A4. First principles computation

The density functional theory was utilized to conduct first-principles calculations, employing the plane-wave basis set Vienna *ab initio* simulation package[39] (VASP). The exchange and correlation functionals were based on Perdew–Burke–Ernzerhof generalized gradient approximation (GGA-PBE).[40]

As for interface stability, the interface was considered as a pseudo-binary of Li_xSi ($x = 0$–4.4) and Li_6PS_5Cl as in previous study.[30] To quantify the thermodynamic driving force, the reaction energy ΔE_R for the interface reactions was calculated as

$$\begin{aligned}&\Delta E_R\left(Li_6PS_5Cl, Li_xSi, a\right)\\ =\ & E_{eq}\left(C_{interface}\left(Li_6PS_5Cl, Li_xSi, a\right)\right)\\ &-E_{interface}\left(Li_6PS_5Cl, Li_xSi, a\right)\\ &-a\cdot\Delta E_R\left(Li_6PS_5Cl\right)-(1-a)\cdot\Delta E_R\left(Li_xSi\right),\end{aligned}\tag{A2}$$

where $C_{interface}$ is the compositions of the interface, normalized to one atom per formula. The a is the molar fraction of Li_6PS_5Cl. The interface phase equilibria were evaluated along the energy minimum. The $\Delta E_{R,min}$ represent the minimum interface reaction energy excluding the decomposition energy of Li_6PS_5Cl and Li_xSi. The energies of most materials were acquired from the Materials Project[30] database.

The electronic band structures and DOS calculations were investigated via the plane-wave-pseudopotential approach based on DFT. All structures were optimized. Then their electronic structures were calculated within the generalized gradient approximation (GGA-PBE), as implemented in the Cambridge serial total energy package (CASTEP) code.[41] The k-point meshes for Brillouin zone sampling were constructed using the Monkhorst–Pack scheme.

Acknowledgments

Project supported by the Major Program of the National Natural Science Foundation of China (Grant No. 22393904), the National Key Research and Development Program of China (Grant No. 2022YFB2502200), Beijing Municipal Science & Technology Commission (Grant No. Z221100006722015), and the New Energy Vehicle Power Battery Life Cycle Testing and Verification Public Service Platform Project (Grant No. 2022-235-224).

References

[1] Janek J and Zeier W G 2016 *Nat. Energy* **1** 16141
[2] Famprikis T, Canepa P, Dawson J A, Islam M S and Masquelier C 2019 *Nat. Mater.* **18** 1278
[3] Cheng X B, Zhao C Z, Yao Y X, Liu H and Zhang Q 2019 *Chem* **5** 74
[4] Gao X, Zhou Y N, Han D, Zhou J, Zhou D, Tang W and Goodenough J B 2020 *Joule* **4** 16
[5] Krauskopf T, Richter F H, Zeier W G and Janek J 2020 *Chem. Rev.* **120** 7745
[6] Wang M J, Kazyak E, Dasgupta N P and Sakamoto J 2021 *Joule* **5** 1371
[7] Tian Y, Zeng G, Rutt A, Shi T, Kim H, Wang J, Koettgen J, Sun Y, Ouyang B, Chen T, Lun Z, Rong Z, Persson K and Ceder G 2021 *Chem. Rev.* **121** 1623
[8] Liu M, Wang C, Cheng Z, Ganapathy S, Haverkate L A, Unnikrishnan S and Wagemaker M 2020 *ACS Mater. Lett.* **2** 665
[9] Janek J and Zeier W G 2023 *Nat. Energy* **8** 230
[10] Tan D H S, Chen Y T, Yang H, Bao W, Sreenarayanan B, Doux J M, Li W, Lu B, Ham S Y, Sayahpour B, Scharf J, Wu E A, Deysher G, Han H E, Hah H J, Jeong H, Lee J B, Chen Z and Meng Y S 2021 *Science* **373** 1494
[11] Franco Gonzalez A, Yang N H and Liu R S 2017 *J. Phys. Chem. C* **121** 27775
[12] Lewis J A, Cavallaro K A, Liu Y and McDowell M T 2022 *Joule* **6** 1418
[13] Sun L, Liu Y, Shao R, Wu J, Jiang R and Jin Z 2022 *Energy Storage Mater.* **46** 482
[14] Cao D, Sun X, Li Y, Anderson A, Lu W and Zhu H 2022 *Adv. Mater.* **34** 2200401
[15] Rana M, Rudel Y, Heuer P, Schlautmann E, Rosenbach C, Ali M Y, Wiggers H, Bielefeld A and Zeier W G 2023 *ACS Energy Lett.* **8** 3196
[16] Yan W, Mu Z, Wang Z, Huang Y, Wu D, Lu P, Lu J, Xu J, Wu Y, Ma T, Yang M, Zhu X, Xia Y, Shi S, Chen L, Li H and Wu F 2023 *Nat. Energy* **8** 800
[17] Cangaz S, Hippauf F, Reuter F S, Doerfler S, Abendroth T, Althues H and Kaskel S 2020 *Adv. Energy Mater.* **10** 2001320
[18] Kato Y, Hori S, Saito T, Suzuki K, Hirayama M, Mitsui A, Yonemura M, Iba H and Kanno R 2016 *Nat. Energy* **1** 16030
[19] Cao D, Ji T, Singh A, Bak S, Du Y, Xiao X, Xu H, Zhu J and Zhu H 2023 *Adv. Energy Mater.* **13** 2203969
[20] Huo H, Jiang M, Bai Y, Ahmed S, Volz K, Hartmann H, Henss A, Singh C V, Raabe D and Janek J 2024 *Nat. Mater.* **23** 543
[21] Son S B, Trevey J E, Roh H, Kim S H, Kim K B, Cho J S, Moon J T, DeLuca C M, Maute K K, Dunn M L, Han H N, Oh K H and Lee S H 2011 *Adv. Energy Mater.* **1** 1199
[22] Huang Y, Shao B, Wang Y and Han F 2023 *Energy Environ. Sci.* **16** 1569
[23] Trevey J, Jang J S, Jung Y S, Stoldt C R and Lee S H 2009 *Electrochem. Commun.* **11** 1830
[24] Wang W and Kumta P N 2010 *ACS Nano* **4** 2233
[25] Chan C K, Peng H, Liu G, McIlwrath K, Zhang X F, Huggins R A and Cui Y 2008 *Nat. Nanotechnol.* **3** 31
[26] Datta M K and Kumta P N 2009 *J. Power Sources* **194** 1043
[27] Tan D H S, Wu E A, Nguyen H, Chen Z, Marple M A T, Doux J M, Wang X, Yang H, Banerjee A and Meng Y S 2019 *ACS Energy Lett.* **4** 2418
[28] Wenzel S, Randau S, Leichtweiß T, Weber D A, Sann J, Zeier W G and Janek J 2016 *Chem. Mater.* **28** 2400
[29] Wenzel S, Leichtweiss T, Krüger D, Sann J and Janek J 2015 *Solid State Ion.* **278** 98
[30] Jain A, Ong S P, Hautier G, Chen W, Richards W D, Dacek S, Cholia S, Gunter D, Skinner D, Ceder G and Persson K A 2013 *APL Mater.* **1** 011002
[31] Zhu Y, He X and Mo Y 2016 *J. Mater. Chem. A* **4** 3253
[32] Grundmann M 2021 *The Physics of Semiconductors, An Introduction including Nanophysics and Applications* 4th Edn. (Cham: Springer International Publishing)
[33] Fang C, Li J, Zhang M, Zhang Y, Yang F, Lee J Z, Lee M H, Alvarado J, Schroeder M A, Yang Y, Lu B, Williams N, Ceja M, Yang L, Cai M, Gu J, Xu K, Wang X and Meng Y S 2019 *Nature* **572** 511
[34] Bao W, Fang C, Cheng D, Zhang Y, Lu B, Tan D H S, Shimizu R, Sreenarayanan B, Bai S, Li W, Zhang M and Meng Y S 2021 *Cell Rep. Phys. Sci.* **2** 100597
[35] Han J, Li H, Kong D, Zhang C, Tao Y, Li H, Yang Q H and Chen L 2020 *ACS Energy Lett.* **5** 1986
[36] Trevey J E, Rason K W, Stoldt C R and Lee S H 2010 *Electrochem. Solid-State Lett.* **13** A154
[37] Piper D M, Yersak T A and Lee S H 2013 *J. Electrochem. Soc.* **160** A77
[38] Asano T, Yubuchi S, Sakuda A, Hayashi A and Tatsumisago M 2017 *J. Electrochem. Soc.* **164** A3960
[39] Kresse G and Furthmüller J 1996 *Phys. Rev. B* **54** 11169
[40] Perdew J P, Burke K and Ernzerhof M 1996 *Phys. Rev. Lett.* **77** 3865
[41] Rehman G, Shafiq M, Saifullah, Ahmad R, Jalali-Asadabadi S, Maqbool M, Khan I, Rahnamaye-Aliabad H and Ahmad I 2016 *J. Electron. Mater.* **45** 3314